OMCat: Catalogue of Serendipitous Sources Detected with the *XMM-Newton* Optical Monitor

K. D. Kuntz[1,2], Ilana Harrus[1,2], Thomas A. McGlynn[2], Richard F. Mushotzky[2], & Steven L. Snowden[2]

Source of Acquisition
NASA Goddard Space Flight Center

ABSTRACT

The Optical Monitor Catalogue of serendipitous sources (OMCat) contains entries for every source detected in the publically available *XMM-Newton* Optical Monitor (OM) images taken in either the imaging or "fast" modes. Since the OM records data simultaneously with the X-ray telescopes on *XMM-Newton*, it typically produces images in one or more near-UV/optical bands for every pointing of the observatory. As of the beginning of 2006, the public archive had covered roughly 0.5% of the sky in 2950 fields.

The OMCat is not dominated by sources previously undetected at other wavelengths; the bulk of objects have optical counterparts. However, the OMCat can be used to extend optical or X-ray spectral energy distributions for known objects into the ultraviolet, to study at higher angular resolution objects detected with *GALEX*, or to find high-Galactic-latitude objects of interest for UV spectroscopy.

Subject headings: catalogues

1. Overview

The Optical Monitor Catalogue (OMCat) contains entries for every point-like source detected in imaging or fast mode OM data. The OMCat was constructed from a complete reprocessing of the Optical Monitor (OM) data using the standard *omichain*/*omfchain* pipelines in SAS 6.5.0. For each observation (ObsID) the reprocessing created a source list; the OMCat is a concatenation of these source lists. Thus, if the same region of sky was observed by multiple ObsIDs, then some sources will be listed multiple times. Each listing should have the same coordinates (to the limit of the astrometric accuracy) and thus it should be reasonably obvious which listings refer to the same source. We have opted to retain multiple listings (rather than to combine them into a "mean" entry) to retain any useful information of temporal variability in an easily accessible manner. An overview of the catalogue statistics is given in Table 1.

In the following document §2 provides a brief description of the OM and its primary observation modes, §3 describes the standard pipeline processing, the further processing done to produce the

[1]The Henry A. Rowland Department of Physics and Astronomy The Johns Hopkins University, 3701 San Martin Drive, Baltimore MD, 21218

[2]Astrophysics Science Division Code 662, NASA/GSFC, Greenbelt, MD 20771

source lists, and the output products that are unique to our processing. §4 contains some useful statistics describing the catalogue. In §5 we demonstrate the extent to which the OM filter set allows photometric classification of point-like sources, and in §6 we explore some of the scientific uses of the OM-specific bands.

2. Brief Description of the OM

The telescope and detector: The OM (Mason et al. 2001) is a 30 cm f/12.7 Ritchey Chretien telescope coaligned with the X-ray telescopes and operating simultaneously with them. The detector is a micro-channel plate intensified charge-coupled device (CCD). Photons striking a photocathode produce electrons that are amplified by two successive micro-channel plates. The electron clouds then strike a phosphor, and the resulting photon splashes are recorded by a CCD; the location of the photon splash is centroided on board. The centroids are stored in units of 1/8 of a CCD pixel. Since it is these photon splashes that are recorded by the CCD, rather than individual photons, the CCD is read out very rapidly (every 11μs), and the centroids of the photon splashes determined and stored. Thus, the CCD is used more like a photon-counting device than an accumulator, although it is an image, rather than an event list, that is produced. The photocathode is optimized for the blue and ultraviolet. The "native" pixel size is $0\farcs476513$ and the point spread function (PSF) FWHM is $1\farcs4$-$2\farcs0$ depending upon filter. The filters are listed in Table 2. The largest possible field of view (FOV) is roughly $17' \times 17'$.

The OM has a smaller FOV than *GALEX* (a 1.2° circle) but better angular resolution (Morrissey et al. 2005, *GALEX* has a $4\farcs5$ FWHM PSF in its FUV filter (1350-1750 Å, and a $6\farcs0$ FWHM PSF in its NUV filter (1750-2800 Å)). The effective areas of the OM and *GALEX* filters are shown in Figure 1 while the OM filter particulars are given in Table 2. Thus, the OMCat data in the UVW2 and UVM2 filters provide an excellent higher resolution complement to the *GALEX* NUV data, while UVW1 data is somewhat redder than the *GALEX* band. The *Swift* UVOT is, essentially, an improved OM, with nearly the same filters, so comparison of data in this catalogue with UVOT data should be straightforward.

The observation modes: Due to the onboard centroiding, memory limitations, and telemetry limitations, setting the OM observation mode has to be a balance of temporal resolution and spatial coverage; the higher the temporal resolution the lower the spatial coverage. As a result, the OM allows a large number of observing modes that place different emphases on temporal and spatial optimization. These modes define different "science windows" covering only portions of the entire FOV; events falling outside of those windows are discarded. There are two primary observation modes at the extremes: the default "imaging" mode and the default "fast" mode.

The default imaging mode consists of five consecutive sub-exposures, each of which employs two science windows; one high-resolution window and one low-resolution window. (Note that resolution, in this case, refers to the degree to which the image is sampled, not to an intrinsic change in the PSF size.) The high-resolution window (roughly $5' \times 5'$) is always located at the center of the FOV. The five low-resolution windows cumulatively cover the entire FOV (roughly $17' \times 17'$) with a center square

surrounded by five rectangular regions. For any number of reasons, not all of the sub-exposures of a default image may actually be taken, but, for the default imaging mode, there will always be a high-resolution sub-exposure for each low-resolution sub-exposure. It should also be noted that if multiple filters are used during a single observation, that the area covered by each filter may be different, depending upon the observation mode. The use of five different science windows to cover the FOV, with some overlap between the windows, means that the exposure is not uniform across the FOV. There are two other common full-field low-resolution modes, "ENG-2" and "ENG-4", which are also included in our processing.

The default fast mode uses the same windows as the default imaging mode with the addition of a third science window (roughly $10\farcs5 \times 10\farcs5$) at an observer defined location (typically the center of the FOV).

The default modes: If the observer did not specify an OM mode, and there was no bright source in the FOV, the OM took exposures in the default imaging mode. For the first two years of the mission the default filters were B, UVW2, U, and UVW1, in order of priority. The filter priority was then changed to UVM2, UVW1, and U, in order to optimize the use of the unique capabilities of the OM.

3. Processing

Image mode processing: For the most part, we have used the standard *omichain* processing with the default settings; exceptions are detailed below. The standard *omichain* processing (processing for images) handles the images produced by each science window separately. For each science window image *omichain* applies a flatfield. The photon splash centroiding algorithm calculates the centroid to 1/8 of a pixel, but due to the algorithm, not all values are equally likely. This problem results in "modulo-8" fixed pattern noise. The *omichain* processing applies a redistribution to correct for this effect.

For every science window image *omichain* runs a source detection algorithm, measures the count rates for the sources, and applies a calibration to convert to instrumental magnitudes. Once all of the science windows are processed, *omichain* produces a "master" source list by combining the source list for each science window, matching sources in common between the lists, and determining the mean (α, δ) for each source. The standard processing has the option to use an external catalogue to correct the coordinates of the master source list; we have used this option with the USNO-B1 catalogue (Monet et al. 2003). It should be noted that the coordinate correction using the USNO-B1 catalogue will fail if there are too few matching sources, in which case no significant solution can be found. The *omichain* algorithm requires at least ten matches in order to produce a significant coordinate correction. If there are too many sources in the field, coordinate correction will also fail, presumably because some fraction of matches are spurious and the solution will not converge. We have found that the coordinate correction *can* fail for almost any density of sources, though we did not determine the cause of that failure.

In addition to combining the source lists for all the filters, *omichain* mosaics the low-resolution

science window images (but not the high-resolution science window images) for each filter. The world coordinate system (WCS) of the first science window for a given filter sets the coordinate system of the entire image mosaic. Note that the standard *omichain* processing can correct the master source list, but not the images. Further, the correction using an external catalogue will be applied only if there are at least ten sources. One does have the option of doing the same correction to the individual science windows, but there are often not enough sources in a single science window to perform such a correction. We have applied the correction derived from the external catalogue to the low-resolution mosaics. Since the mosaic images use the WCS from the first science window in the mosaic, we compared the (α, δ) in the source list for the first science window to the (α, δ) in the USNO corrected master list. We then determined the $(\Delta\alpha, \Delta\delta)$ which must be added to the (α, δ) of the first source list in order to obtain the (α, δ) in the USNO corrected master list. We then applied that correction to the header keywords of the mosaicked image. Two points must be noted. 1) Since the telescope can drift by 1-2 arcseconds between exposures, this correction is done separately for each filter. 2) There are often not enough sources in a single science window to attempt to determine the offset and rotation that would best align the first source list with the master list. Therefore, we have assumed that the rotation between the master list and the external catalogue can be applied to all of the science windows.

The standard *omichain*[3] processing does not combine the images from the high-resolution science windows. However, we have done so, though not with *ommosaic*, the standard SAS tool. The *ommosaic* program uses the WCS keywords to determine the offsets needed to align the WCS frames of the individual science windows before summing. We allow the WCS of the summed image to be set by the first science window. For each successive high resolution image, we compare the source list to the source list from the first image, determine the $(\Delta\alpha, \Delta\delta)$ required to match the source lists, and apply that offset to the image before adding it to the mosaic. Not all sources are used for determining the offsets, only sources appearing in at least half of the images; this selection removes sources with poorly determined positions. The offsets are rounded to the nearest integer pixel; subpixelization did not seem to produce a sigificant improvement in the resultant PSF, and so was not used for this processing. Compared to the direct sum of the images made by *ommosaic*, our processing does improve the PSF of the summed image, sometimes improving the FWHM by as much as a pixel (see Figure 2). We compare the source list from the first image with the master source list to correct the summed image in the same manner used for the low-resolution mosaics.

Further coordinate correction: After our initial processing of the public archive we found that the pipeline coordinate correction (done by *omichain*) using the USNO catalogue failed for $\sim 38\%$ of the fields. Further, the failure was not limited to extremely high or extremely low source densities (see Figure 3)[4]. We thus found it worthwhile to create our own coordinate correction routine (the "post-pipeline" correction) using the USNO catalogue. Although the bulk of fields need only a small correction, some fields need substantial corrections ($\sim 2''$). Thus, although we attempt to find

[3]SAS routines are documented at http://xmm.vilspa.esa.es/sas/6.5.0/doc/packages.All.html

[4]We have not had the opportunity to trace the root of this problem. However, we note that a disproportionate number of ObsIDs lacking pipeline corrections *seemed* to have a single science window that was strongly discrepent from the others.

high precision corrections for all fields, it is still worthwhile to find lower accuracy corrections for those fields that do not have a large enough number of matches with the USNO catalogue to attempt a high precision solution.

We used a fairly simple and robust algorithm for matching the OM sources to the USNO sources. If there were > 10 matches we iteratively solved for the offset in (α, δ) that minimized the offset between the OM source list with the USNO source list. By iterating the solution we could eliminate some portion of the false matches. We have not solved for a rotation for two reasons: 1) adding a rotation to the fit did not significantly improve the solution, and 2) given that there are systematic offsets from one science window to another, the rotation could be strongly biased by the offset of a single science window. If there were $3 < n < 10$ matches we merely calculated the mean offset between the OM and USNO sources, and used that offset as the coodinate correction. If there were < 3 sources we did not attempt a correction. We applied the same correction to the individual images that we applied to the source lists.

For each OM source in the source list with a significance in any filter > 3, the matching algorithm finds the closest USNO source. It then creates the distribution of the distances between the OM sources and their closest USNO counterparts. If all of the OM sources had USNO counterparts, then this distribution would be a Gaussian whose width is the coordinate uncertainties of the two catalogues and whose peak is the offset between the two catalogues. If there were no true matches between the OM sources and the USNO catalogue, then the distribution would be given roughly by the probability distribution for the minimum distance between a given point and a uniform distribution of sources:

$$P(r) = e^{\left[-\rho\pi r^2\right]}\rho\pi[(r+\delta r)^2 - r^2]e^{\left[-\rho\pi[(r+\delta r)^2 - r^2]\right]} \quad (1)$$

where ρ is the surface density of sources and δr is the binsize of one's histogram of distances. For this distribution both the peak of the distribution and the width of the distribution scale as $\rho^{-0.5}$. We expect that some fraction of the OM sources have true USNO matches and that the remainder will not. As a result, the observed distribution of sources has a sharp peak with a width of $\sim 0.3''$ due to matches and a low, broad distribution for the spurious matches. This algorithm has problems with high density regions; for source densities of 5000 sources/image (0.005 sources arcsec^{-2}), the distribution of spurious matches peaks at $6.3''$ with the lower half-maximum at $2''$. Although the peak of the matching sources typically has $r \lesssim 3''$, the true match rate is likely to be small compared to the spurious match rate, and so it is difficult, if not impossible, to find the true match peak in this distribution. However, at these source densities, source confusion is a serious problem as well, so even if the matching algorithm worked, the coordinate solution would remain problematic.

For the matching algorithm, we simply fit the distribution with a Gaussian. If the width of the Gaussian is smaller than $0\farcs7$, then the algorithm takes all of the sources within 3σ of the peak of the distribution as real matches. An initial solution is determined from those matches, and a fit is made in the image coordinate frame to find the (α, δ) offset that minimizes the distance between the OM sources and their USNO matches. The source matching is redone with the new offset, and the process is iterated until it converges. After application of our coordinate correction routines, only $\sim 14\%$ of the fields remained without any coordinate correction. Besides fields with very few objects, the fields without coordinate corrections were characterized by very broad distribution of the matches

suggesting a combination of large pointing error and large source density, and thus a large number of spurious identifications.

For fields where the pipeline processing found a good coordinate solution using the USNO catalogue our coordinate correction was not significantly different. However, our coordinate correction did improve the mean distance between OM and USNO sources for $\sim 44\%$ of fields, and provided the only coordinate corrections for $\sim 23\%$ of fields.

The RMS residual between the OM sources and the matching USNO sources was calculated for every field. A value of zero indicates that there was no coordinate solution. Coordinate solutions with RMS residuals $> 0\farcs6$ should be considered to be poor.

Fast mode processing: The bulk of the fast mode processing is concerned with the production of light-curves of the source. The fast mode images consist of $10\farcs5 \times 10\farcs5$ regions containing, typically, a single source. We combine all of the images for each filter using the same method applied to the high-resolution images.

Further processing: Further processing is required to provide a more useful source list to be incorporated into the OMCat. To the standard image catalogue (a binary fits table) we add images of each source from each filter. Each "postage stamp" image is 19×19 pixels in size, extracted from the low-resolution image mosaics (the pixel size is $0\farcs95$ and the image is $18\farcs1 \times 18\farcs1$ in size). Since the sources were derived from all of the science windows, some sources can fall in high-resolution science windows without low-resolution counterparts. In that case the postage stamp is extracted from the high-resolution image and binned to the same resolution and size as the other postage stamps. Sources that appear only in "fast" science windows are treated similarly. Note that postage stamps are extracted from all of the available filters, not just the filters for which the source was detected; many postage stamps may thus appear to be empty.

Processing summary: For each ObsID our processing produces a coordinate corrected source list, a coordinate corrected low-resolution mosaicked image for each filter, a coordinate corrected high-resolution mosaicked image for each filter (if possible), or a summed fast mode image.

Caveats: 1) Individual science windows may be significantly offset (1-2″) from the remainder of the mosaic. In this case the correction by use of the USNO-B1 catalogue will not be wholly satisfactory, and sources will appear to be offset in the postage stamps. The extent of this problem for any individual source can determined by looking at the "RMS_RESID" column which contains the RMS residual from the fit of source list to the USNO-B1 catalogue.

2) The source lists will contain spurious sources; sources due to ghost images, diffraction spikes, readout streaks, saturation around bright sources, and other effects. Some of these sources can be removed by consulting the Q_FLAG parameter Similarly, confused sources are flagged by the C_FLAG parameter. However, we have found that filtering out sources with significances less than three was a more efficient means of removing spurious sources than reference to the quality flags.

3) Although we provide the mosaicked low-resolution and mosaicked high-resolution images through the archive, these images, according to the SAS documentation, should not be used for photometry. There are a number of corrections in the photometric reduction which can not be made

from the mosaicked images. However, since coincidence-loss and dead-time corrections should be small for faint extended emission, photometry of such sources, which is not trivial in SAS, should, in principle, be possible from the mosaics.

4) Although there may be substantial exposure for a given mosaic, the detection limit in the current catalogue is not substantially better than for a lower exposure mosaic since the source detection is done on the individual science windows rather than on the mosaicked images. Since the individual science windows have a mean exposure of ~ 2200 s, and the bulk of the individual science windows have exposures of 1000 s, the detection limit of the OMCat is more uniform but somewhat lower than one would expect from the mosaic exposure times.

Availability: The bulk of the data in the OMCat can be accessed either through the Browse facility at the High Energy Astrophysics Archive (HEASARC) or through the Multimission Archive at STScI (MAST). Slightly more information for each source (shape, confusion flags, and quality flags, as a function of filter) are retained in the source lists for individual ObsIDs, and can be downloaded from the HEASARC with the rest of the OM data.

4. OMCat Statistics

Observation Statistics: Of the 4373 observations that were public by 1 September 2006, 2950 observations had OM imaging mode data and 202 had OM fast mode data. About 25% of the fields imaged were observed more than once, allowing some measure of temporal variability. However, the number of fields with multiple observations is a very strongly declining function of the number of repetitions (see Figure 4).

The Galactic plane has a high density of observations (particularly towards the Galactic center), the region with $|b| < 30°$ has a lower density of observations, and the region with $|b| > 30°$ is relatively uniform, though Coma and the Magellanic clouds have visible concentrations of observations (Figure 5). The imaging mode observations cover a cumulative $\sim 0.5\%$ of the sky.

Figure 6 shows the distribution of total exposure time per field and the exposure time per science window as a function of filter. Most science windows have exposures of a kilosecond, while the total exposure per field is significantly higher. Thus, since the point source detection is done in the individual science windows, the OMCat could be made significantly deeper were point source detection to be executed on mosaicked images. However, since the bulk of individual science window exposures are ~ 1000 seconds, the catalogue depth is relatively uniform. Figure 7 shows the distribution of magnitudes for each filter.

Figure 8 shows the distribution of the residuals between the corrected source catalogues and the USNO-B1 catalogue for those fields for which a coordinate correction was successful. The residuals before the post-pipeline correction are peaked around $0\farcs4$ with a secondary peak around $0\farcs7$. After correction, the distribution is more symmetrically distributed around $0\farcs4$. It should be noted that a portion of the residual for any given image can be due to the offset of individual science windows within the mosaic.

The distribution of the calculated offsets between coordinates before and after the post-pipeline correction by the USNO catalogue is shown in Figure 9. The distribution is a broad skewed Gaussian peaking at $\sim 1\farcs7$ with a significant tail extending to $\gtrsim 5''$. Note that this distribution does not reflect the pointing ability of the telescope, but rather the performance of the tracking corrections in the OM pipeline.

Source Statistics The OMCat contains roughly 3.7×10^6 entries, of which 82% have detection significance greater than three (as determined by maximum likelihood calculations in the pipeline processing) in at least one band and 72% have S/N greater than three in at least one band. Roughly 71% of all entries have had successful coordinate corrections. Only $\sim 3.7\%$ of sources are classified as extended; the rest are considered point-like. Approximately 60% of the sources are flagged for data quality in at least one band, and approximately 74% of the sources are flagged for confusion in at least one band. However, these flags are applied rather conservatively, so the true number of sources/measurements affected are significantly lower.

Due to the interests of observers and the changing default filter priorities, the distribution of exposures among the various filters is uneven. When measured in terms of the number of sources with 3σ detections in each filter, the U-UVW1, V-B, and B-U colors have the best statistics. Table 3 shows the number of sources with 3σ detections for each filter and filter combination. As one might expect, the distribution for X-ray selected sources (that is, X-ray point sources in the field with OMCat counterparts rather than just sources observed because of their X-ray properties) is somewhat different, with U-UVW1, B-U, B-UVW1, and UVW1-UVM2 having the best statistics.

5. Properties of the OM Filters

The OM unique filters are UVW1, UVM2, and UVW2, in order of decreasing throughput (see Figure 1). In order to explore the abilities of the OM filters, we created U−UVW1 *vs.* UVW1−UVM2 and U−UVW1 *vs.* UVW1−UVW2 color-color diagrams of the sources in the OMCat (Figure 10). On those diagrams we have plotted the expected locus for dwarf stars (solar metallicity stars from the 1993 Kurucz atlas[5]), as well as points representative of galaxies (taken from the Kinney & Calzetti atlas at STScI[6] see Kinney et al. (1996)) and AGN (taken from STScI AGN atlas collection of spectra[7] see Francis et al. (1991)). The conversion from spectra to photometric colors was made using the OM spectral response matrices available from the *XMM-Newton* SOC[8].

It is immediately apparent that the OM colors are a good match to those expected from the Kurucz atlas, except for the stars later than about G5. This problem appears most clearly in the U-UVW1 *vs.* UVW1-UVW2 diagram, but appears as well in the V-B *vs.* B-U diagram. The problem

[5]http://www.stsci.edu/hst/observatory/cdbs/k93models.html

[6]http://www.stsci.edu/hst/observatory/cdbs/cdbs_kc96.html

[7]http://www.stsci.edu/hst/observatory/cdbs/cdbs_agn.html

[8]ftp://xmm.esac.esa.int/pub/ccf/constituents/extras/responses/OM

region is off the bottom of the U-UVW1 *vs.* UVW1-UVM2 diagram. The true nature of the problem is not yet clear. For much of the stellar tracks the reddening vectors are roughly parallel to the stellar track.

There is a strong overlap between the early dwarf stars (down to A5) and AGN, as well as somewhat later dwarf stars (A5 to F5) and typical galaxies. There is no way to distinguish early stars from AGN using the UV colors alone, and the UV colors of QSO do not change much with redshift. The AGN seem to be more offset from the early-type stars in the optical color-color diagram. Given the extinction in the UV, it would be unreasonable to expect to find AGN in regions with early type stars, though the converse is not necessarily true, and indeed, finding high latitude O and B stars would be interesting. Division of sources into low ($|b| < 30°$) and high ($|b| > 60°$) Galactic latitude samples shows that in the UV color-color diagram the early type star region is populated somewhat more strongly at higher Galactic latitudes while the later type star region is populated somewhat more strongly at lower Galactic latitudes. We have cross-correlated the OMCat with the Veron QSO catalogue and the SDSS QSO catalogue and found that the objects in common lie in the expected locations in the color-color diagram (Figure 11).

As can be seen in Figure 12, the cross-correlation of the CfA redshift survey with the OMCat suggests that the sources falling within the matching radius will be strongly contaminated by false-matches (at the $\sim 20\%$ level), meaning that many OMCat stellar sources will be falsely matched to the CfA survey. This high false-matching rate is presumably due to the fact that the CfA redshift survey has a very high density of objects that are much fainter than those detected in the OMCat. However, the matching sources from the CfA redshift survey fall at the expected location in the color-color diagrams, though their scatter may be a bit larger than the other surveys.

6. Uses of the OMCat

The uses of the OMCat detailed here involve the cross-correlation of the OMCat with other catalogues. All the catalogues were extracted from the HEASARC Catalogue Resources using the HEASARC Browse tool[9]. The cross-correlation for a given catalogue was done by determining the closest entry to each OMCat source. We then plotted the distribution of the distances between the OMCat source and the closest catalogue source. Cross-correlation of the OMCat with catalogues with a high density of sources typically produced a distribution of distances with a strong peak at $\sim 0.2-0.3$ arcseconds and a FWHM of $\sim$0.3 arcseconds, and a tail due to serendipitous matches; the higher the density of catalogue sources, the higher the serendipitous match rate at large distances. An OMCat source was generally considered to be matched if the distance between it and the catalogue source was less than the peak of the distribution $+2\sigma$. The catalogues and match criteria used are shown in Table 4 while the distributions are shown in Figure 12.

[9]The USNO-B1.0 and 2MASS catalogues are maintained by the VizieR service of the Centre de Données Astronomiques de Strasbourg and were accessed through the HEASARC Browse interface.

6.1. USNO Counterparts

Most of the sources in the OMCat have USNO counterparts. This suggests that the OMCat is shallower in the UV than the USNO is in the B and R bands. The OMCat is therefore not dominated by sources previously undetected at other wavelengths.

6.2. FUSE Counterparts

Of interest to studies of the halo of the Galaxy are UV-bright stars and AGN that can be used as background sources for measuring the column density, velocity, and metallicity of halo gas. Stars are of use in determining the distance to high and intermediate velocity gas (e.g., Danly et al. 1993), while AGN provide measures of the column density through the entire halo. Targets are usually found by combing catalogues of sources for objects with optical colors suggesting high UV fluxes. Since the fields in the OMCat were (usually) chosen for their X-ray sources, rather than the UV sources in the same field, comparing the UV sources in the OMCat with the types of catalogues that have been used in the past to find UV-bright objects provides an indication of how many UV-bright sources may have been missed.

We have cross-correlated the OMCat with several UV catalogues; the *GALEX* catalogue, the Far Ultraviolet Explorer (*FUSE*) observation log (not technically a catalogue), and the TD1 catalogue; the offset distributions are shown in Figure 12. We also cross-correlated with the Far-UV Space Telescope (*Faust*) Far-UV Point Source Catalogue, but did not find any matches, likely due to the small number of sources in that catalogue. There are a number of other EUV catalogues from *EUVE* and the *ROSAT* WFC, but the position uncertainties are $\gtrsim 1'$, so they are not useful for this study.

A significant interest with UV catalogues is the *FUSE* observation log, given that *FUSE* is still operational. The top panels of Figure 13 show the OM color-color diagram with the *FUSE* matches marked in red and coded by source type. AGN from a number of other catalogues have also been plotted. The bulk of the matching *FUSE* observations with matching OM sources are AGN. The difficulty is that the AGN, early type stars, extragalactic star-forming regions, and some galaxies overlap in these color-color plots. We can define a long rectangular region along the early type star track as being dominated by stars. Below and to the right is a large irregular region that has a significant population of AGN. From the available data we can not estimate the contamination of the "AGN" region by stars, or the "stellar" region by AGN. The extragalactic star formation regions and a handful of small galaxies can be easily removed by visual inspection of the images. The lower panels of Figure 13 show the OM UVW1 and UVM2(UVW2) magnitudes of the sources. Again, the OM sources matching *FUSE* observations have been marked in red and coded by *FUSE* type. The OM source matching *FUSE* observations have U and UVW1 magnitudes $\gtrsim 18.5$, which suggests sources that are well detected by the OM should be observable by *FUSE*.

In the region with $|b| > 46°$ where Galactic absorption is generally small, we have identified 52 potential AGN accessible to *FUSE* (i.e., in the selection region with instrumental magnitudes < 18.5 in the U and UVW1 bands and not previously observed with *FUSE*), two lie in the direction of High/Intermediate Velocity Clouds, and another four lie sufficiently close to clouds to be of interest.

We have identified 80 potential upper main sequence stars accessible to *FUSE* (i.e., in the selection region with instrumental magnitudes < 18.5 in the U and UVW1 bands and not previously observed with *FUSE*), four lie in the direction of High/Intermediate Velocity Clouds, and another six lie sufficiently close to clouds to be of interest. It should be noted, especially for the fainter sources, that repeated observations (such as those of the Lockman Hole) will produce somewhat different colors, moving a source in and out of the AGN selection region.

6.3. X-ray Counterparts

6.3.1. Matching the Catalogues

We matched the *XMM-Newton* Serendipitous Source Catalogue (SSC, The Second XMM-Newton Serendipitous Source Pre-release Catalogue, *XMM-Newton* Survey Science Centre, 2006) against the OMCat. We first filtered out all of the *XMM-Newton* serendipitous sources that did not fall within the field of view of the corresponding OM observation. Because we did not know the relative positional uncertainty to expect when comparing the X-ray detections with the OM detections, we matched the SSC to the OMCat in the same way that we matched the USNO catalogue to the OMCat. The distribution of the distance between the X-ray sources and the closest OM source is shown in Figure 14; the sharp peak at $\sim 0.5''$ is presumably due to true matches between X-ray and OM sources while the broader peak is due to uncorrelated sources. In order to determine the extent to which our matches are contaminated by serendipitous alignments, we calculated the probability distribution of Equation 1 for each source in the SSC that fell within the OM FOV using the density of OM sources in the FOV for the observation containing the SSC source. Because some of the SSC sources do have real matches, this calculation over-estimates the probability distribution of serendipitous matches. In order to correct for this over-estimation, we assumed that sources with distances of $r < 8''$ had a non-negligible probability of being real matches. We then summed over the probability distribution for $r > 8''$ and normalized that to the total number of matches found with $r > 8''$. We then used this normalized model distribution to determine the fraction of matches at distance r which are due to serendipitous coincidences of uncorrelated sources.

We have taken as "real" X-ray-OMCat matches all those with distances $r < 2''.5$. At $r = 2''.5$ there are still four times as many real matches as there are random coincidences but the contamination rate for $r < 2''.5$ is $\sim 10\%$. Of the 53848 sources from the XMM Serendipitous Source catalogue falling within the FOV of the corresponding OM observations and having coordinate corrections from the USNO, 12986 have OM source counterparts, of which 1092 are expected to be spurious. It should be noted that in matching the X-ray sources to the OM sources, the USNO corrected coordinates provide a much closer match than do the original OM coordinates.

6.3.2. Results

The bulk of the X-ray sources are expected to be background AGN and Galactic stars. Given the observational interest in galaxies, there will also be a small, probably negligible, contribution

from extragalactic X-ray binaries and star-forming regions. The question of interest when comparing catalogues at different energies is whether the X-ray sources detected in the UV fall in distinctive portions of X-ray/UV color/hardness diagrams. Figure 15 compares the U-UVW1 color (the UV color for which we have the greatest number of sources) with the 2.0-12.0/0.5-2.0 keV X-ray hardness. From Figure 10, we expect AGN to have U-UVW1$\sim$ 0.4 and stars to have U-UVW1$<$ 0. The same behavior is observed in the color-hardness diagram, with an additional separation in X-ray hardness; the X-ray sources with UV colors of AGN have Log(Hard)-Log(Soft) peaked around 0.2 and the X-ray sources with UV colors of stars have a broad distribution peaking at Log(Hard)-Log(Soft)$<$ 0. This distribution reflects the well understood difference between the soft thermal X-ray spectra of stars and the harder power-law X-ray spectra of AGN. The combination of X-ray and UV colors are probably a more powerful star-AGN discriminator than either alone. The diagonal line in Figure 15 marks a reasonable separation between these two categories.

To test this separation we have cross-correlated the sources with good X-ray and UV data with the SDSS catalogue of sources with classifications made from optical spectra. Indeed, the AGN (blue) are clustered as expected. The bulk of the galaxies (green) have stellar colors, but many have AGN-like colors. Since the SDSS sources chosen for spectroscopy were selected to have a low probability of being stars, based on their colors and being unresolved, the low number of stars (red), and that fact that they have AGN-like colors, should not be surprising.

The contours in Figure 16 show the density of SSC catalogue sources in the Hard (2.0-12.0 keV) *versus* Soft (0.5-2.0 keV) band space; the points show the locations of sources with U-UVW1 colors. Not surprisingly, many of the sources with only soft X-ray detections have UV detections while there are only a few sources that have only hard X-ray detections that also have UV detections. The hard X-ray sources with UV detections tend to have AGN-like colors. To state it in the converse, very few hard X-ray sources (i.e., strongly absorbed sources) have UV counterparts.

The SSC sources with UV counterparts that also have QSO counterparts in the SDSS spectroscopic survey are shown in Figure 17. The sources cluster along the tracks expected if the X-ray and UV flux are related by

$$\log_{10} L_{2keV} = \log_{10} L_{2500\mathring{A}} + \alpha_{OX} + \log_{10} \frac{\nu_{2keV}}{\nu_{2500\mathring{A}}} \quad (2)$$

where $\alpha_{OX} = 1.35$ and the photon index of the X-ray spectrum is taken to be $\Gamma = 2.0$. We have plotted tracks for QSOs with unabsorbed $10^{43} < L_{2keV} < 10^{47}$ both with internal absorption of $N_H = 10^{24}$ cm^{-2} and without internal absorption. There is a large amount of scatter, and some slight suggestion that the low redshift objects are X-ray bright compared to the model. It should be noted that this sample of sources (*XMM-Newton* X-ray sources with OM counterparts and SDSS spectroscopic survey counterparts) seems to be a relatively unbiased sample of the SDSS spectral catalogue; the distribution of spectroscopic classification and redshift in the sample matches the distribution of all of the sources in the 12′ radius SDSS spectroscopic catalogue extracts centered on the OM pointing directions.

7. Summary

The OMCat provides a quick source of photometric data of point-like sources in the optical and near ultra-violet over an increasing fraction of the sky. The OMCat will continue to be augmented at the HEASARC as the *XMM-Newton* data becomes public. Although the short average exposure places a relatively high detection limit compared to optical catalogues such as USNO-B, the current detection limit provides suitably bright targets for current UV spectrometers, and provides high angular resolution data suitable for meaningful comparison with *GALEX* images. A first glance at the AGN counterparts in the OMCat suggests their UV properties are not particularly unexpected. No doubt more targeted querying of the OMCat will produce interesting science in several different fields.

We would like to thank Mike Arida for his help in making the OM data available through the HEASARC. We would like to thank Karen Levay, Randy Thompson, and Rick White for their help in making this data MAST accessible. We would like to thank Luciana Bianchi for many useful discussions, as well as B.G. Anderson for his help with *FUSE*. We would also like to thank Lorenzo Principe for his help with this work.

This research used data obtained the Browse facility of the High Energy Astrophysics Science Archive Research Center (HEASARC). The OM object catalog is now available through Browse [10] and in a static ASCII version[11]. Several databases accessed through browse are actually held by the *VizieR* service at http://vizier.u-strasbg.fr. (Ochsenbein et al. 2000).

This research has made use of data from the *XMM-Newton* Serendipitous Source Catalogue, a collaborative project of the *XMM-Newton* Survey Science Center Consortium, http://xmmssc-www.star.le.ac.uk.

This research has made use of the *GALEX* GR2/GR3 database/archive at the Multimission Archive at STScI (MAST). STScI is operated by the Association of Universities for Research in Astronomy, Inc., under NASA contract NAS5-26555. Support for MAST for non-HST data is provided by the NASA Office of Space Science via grant NAG5-7584 and by other grants and contracts.

This research has made use of data obtained from Data Release 5 of the Sloan Digital Sky Survey (SDSS). Funding for the Sloan Digital Sky Survey has been provided by the Alfred P. Sloan Foundation, the Participating Institutions, the National Aeronautics and Space Administration, the National Science Foundation, the U.S. Department of Energy, the Japanese Monbukagakusho, and the Max Planck Society. The SDSS Web site is http://www.sdss.org/. The SDSS is managed by the Astrophysical Research Consortium (ARC) for the Participating Institutions. The Participating Institutions are The University of Chicago, Fermilab, the Institute for Advanced Study, the Japan Participation Group, The Johns Hopkins University, Los Alamos National Laboratory, the Max-Planck-Institute for Astronomy (MPIA), the Max-Planck-Institute for Astrophysics (MPA), New

[10] http://heasarc.gsfc.nasa.gov/docs/archive.html

[11] http://heasarc.gsfc.nasa.gov/FTP/heasarc/dbase/tdat_files/ heasarc_xmmomcat.tdat.gz

Mexico State University, University of Pittsburgh, Princeton University, the United States Naval Observatory, and the University of Washington.

REFERENCES

Danly, L., Albert, C. E., & Kuntz, K. D. 1993, ApJ, 416, L29

Fitzpatrick, E. L. 1999, PASP, 111, 63

Francis, P. J., Hewett, P. C., Foltz, C. B., Chaffee, F. H., Weymann, R. J., & Morris, S. L. 1991, ApJ, 373, 465

Kinney, A. L., Calzetti, D., Bohlin, R. C., McQuade, K., Storchi-Bergmann, T., & Schmitt, H. R. 1996, ApJ, 467, 38

Mason, K. O., et al. 2001, A&A, 365, L36

Monet, D. G., et al. 2003, AJ, 125, 984

Morrissey, P., et al. 2005, ApJ, 619, L7

Ochsenbein, F., Bauer, P., & Marcout, J. 2000, A&AS, 143, 221

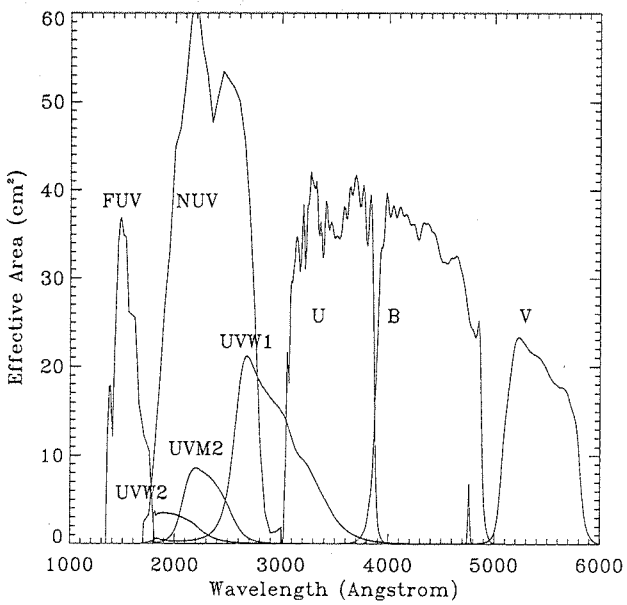

Fig. 1.— The two lowest wavelength filters are the *GALEX* FUV and NUV filters. The next three are the OM UVW2, UVM2, and UVW1 filters. The three highest wavelength filters are the OM U, B, and V filters.

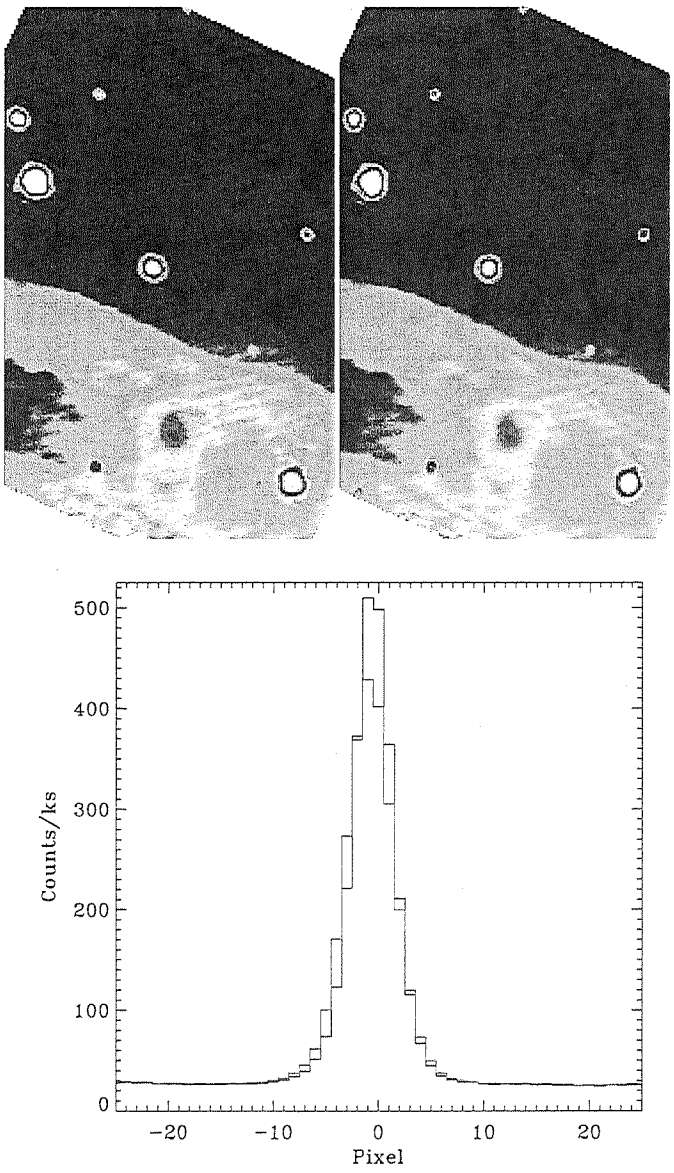

Fig. 2.— **Top:** Image created from the 25 high-resolution science windows using *ommosaic* (left panel) compared to the same image created with our processing (right panel). Note that the central point source is rounder after our processing, and a number of knots of faint emission are more clearly visible. **Bottom:** Comparison of the profile of the central point source *red:* with *ommosaic* alone *black:* with our processing. The FWHM improves by almost a pixel in this case and the peak intensity increases by 15%.

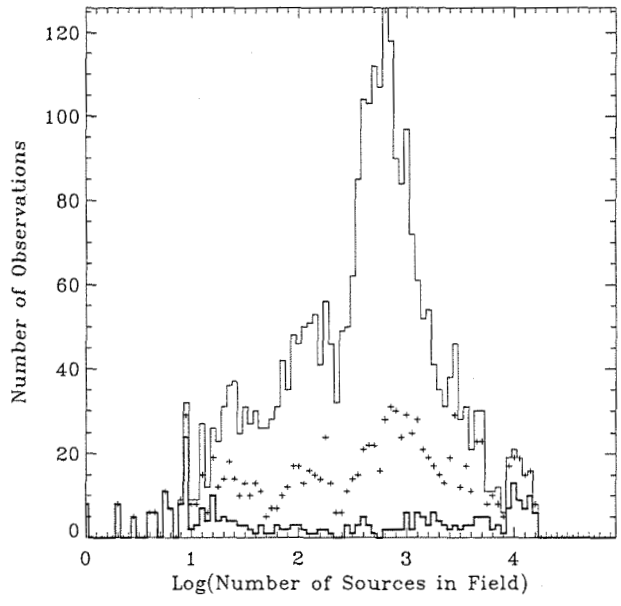

Fig. 3.— Histogram of the number of sources detected in each field. The crosses (red) show the number of fields for which the pipeline coordinate correction (i.e., that done by the SAS *omichain* task) failed as a function of the number of sources. The thick(blue) line shows the number of fields for which the post-pipeline coordinate correction (our software) failed as a function of the number of sources.

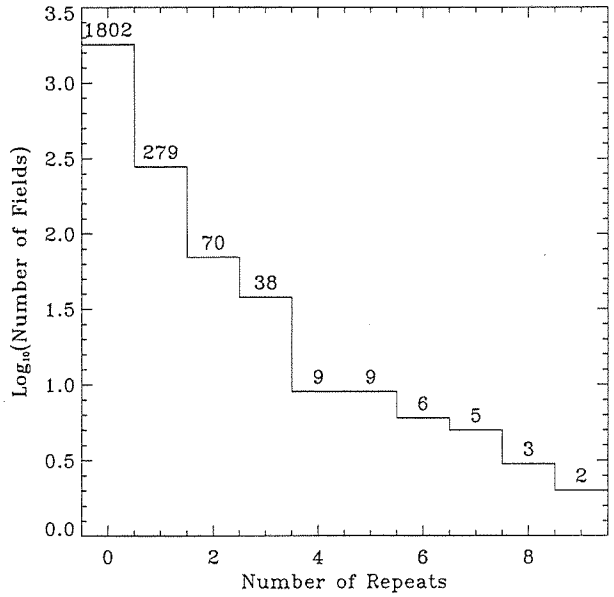

Fig. 4.— The histogram of the number of fields as a function of the number of times that the observation was repeated. Obervations were considered to be repeated if the pointing directions between two observations were offset by no more than half an arcminute. Zero repeats indicates a field with only one observation. The numbers give the number of fields for each number of repetitions.

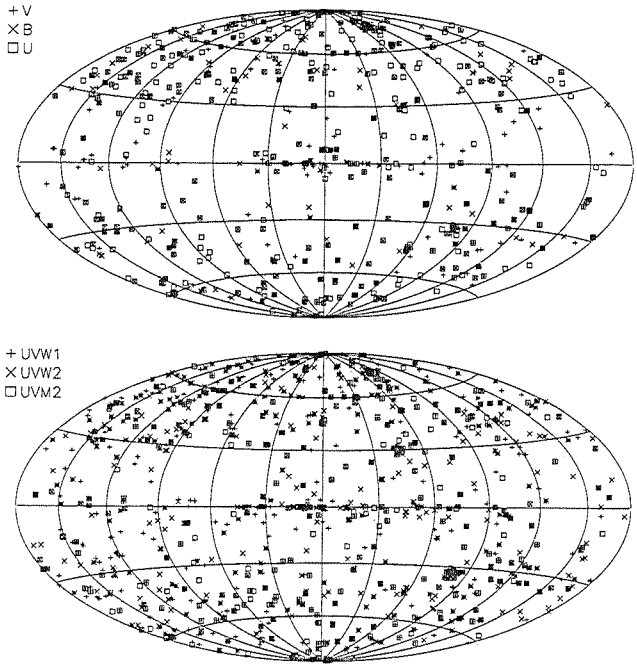

Fig. 5.— The distribution of observations over the sky. The Aitoff coordinate system is centered on $(\ell, b) = (0°, 0°)$ with positive longitudes towards the left.

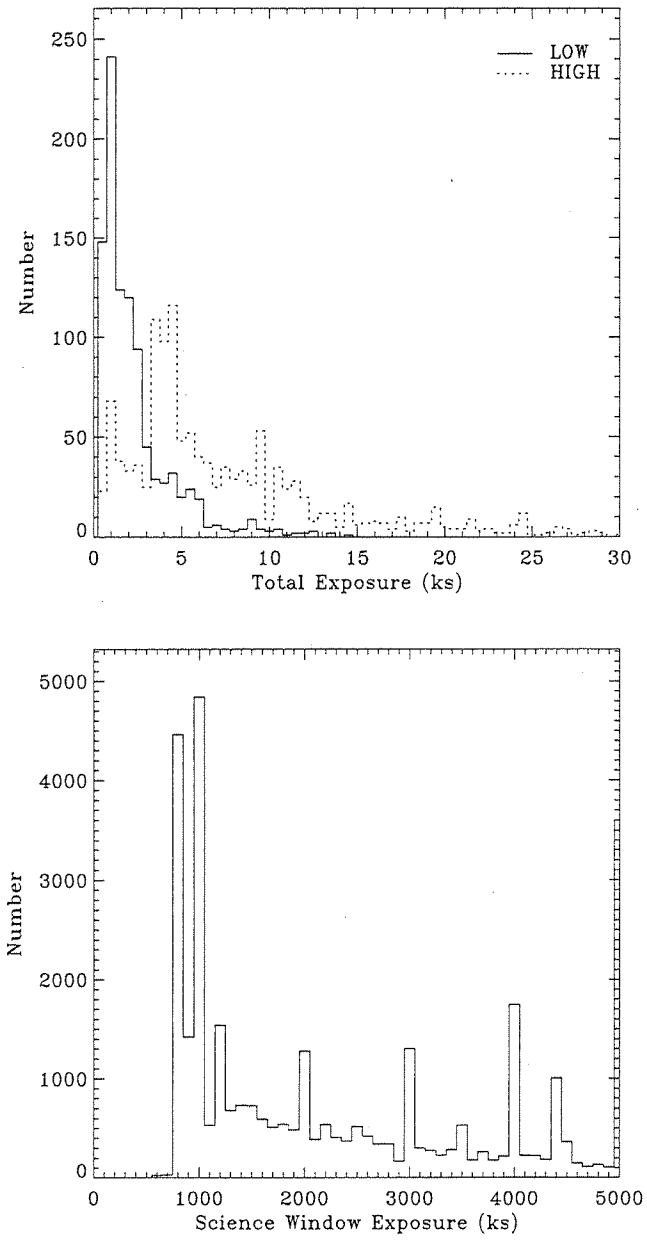

Fig. 6.— *Top:* The distribution of the exposure times for the UVW1 filter. Other filters have not been used as much as the UVW1 filter, so their values will be lower. The solid line is the distribution of the mean exposure time low-resolution mosaic (since the exposure time will vary over the mosaic) and the dotted line is the distribution of exposure time for the sum of the high resolution image centers. *Bottom:* The distribution of exposure times for individual science windows.

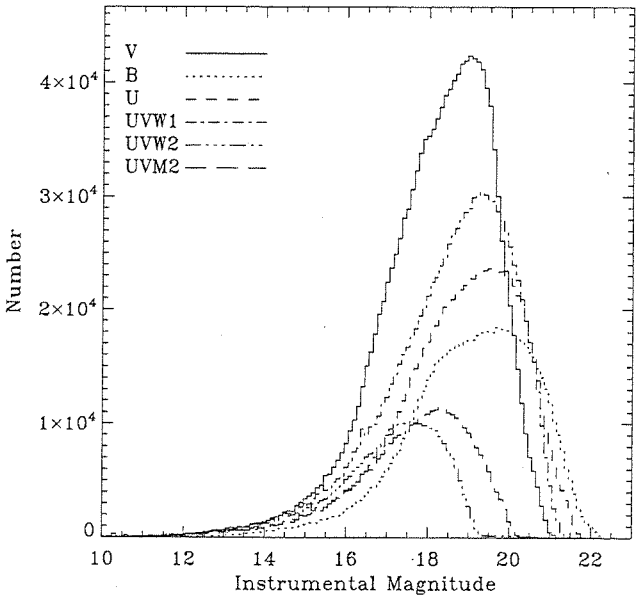

Fig. 7.— The histogram of the numbers of sources at each magnitude for each of the filters. Only sources with $> 3\sigma$ detections have been counted.

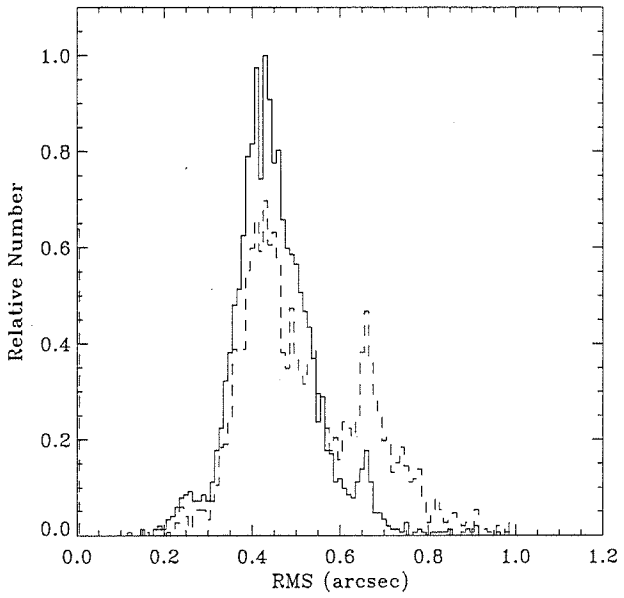

Fig. 8.— The histogram of the resultant R.M.S. residuals between the corrected source catalogue and the USNO-B1 catalogue for those fields for which a coordinate correction was successful. *Solid:* Relative number of fields after the post-pipeline correction. *Dashed(red):* after the pipeline correction.

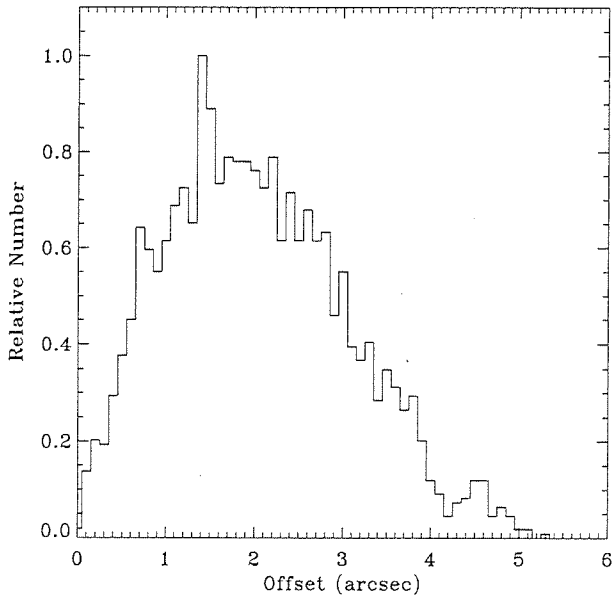

Fig. 9.— The histogram of the magnitude of the shifts introduced by the correction to USNO-B1 coordinates.

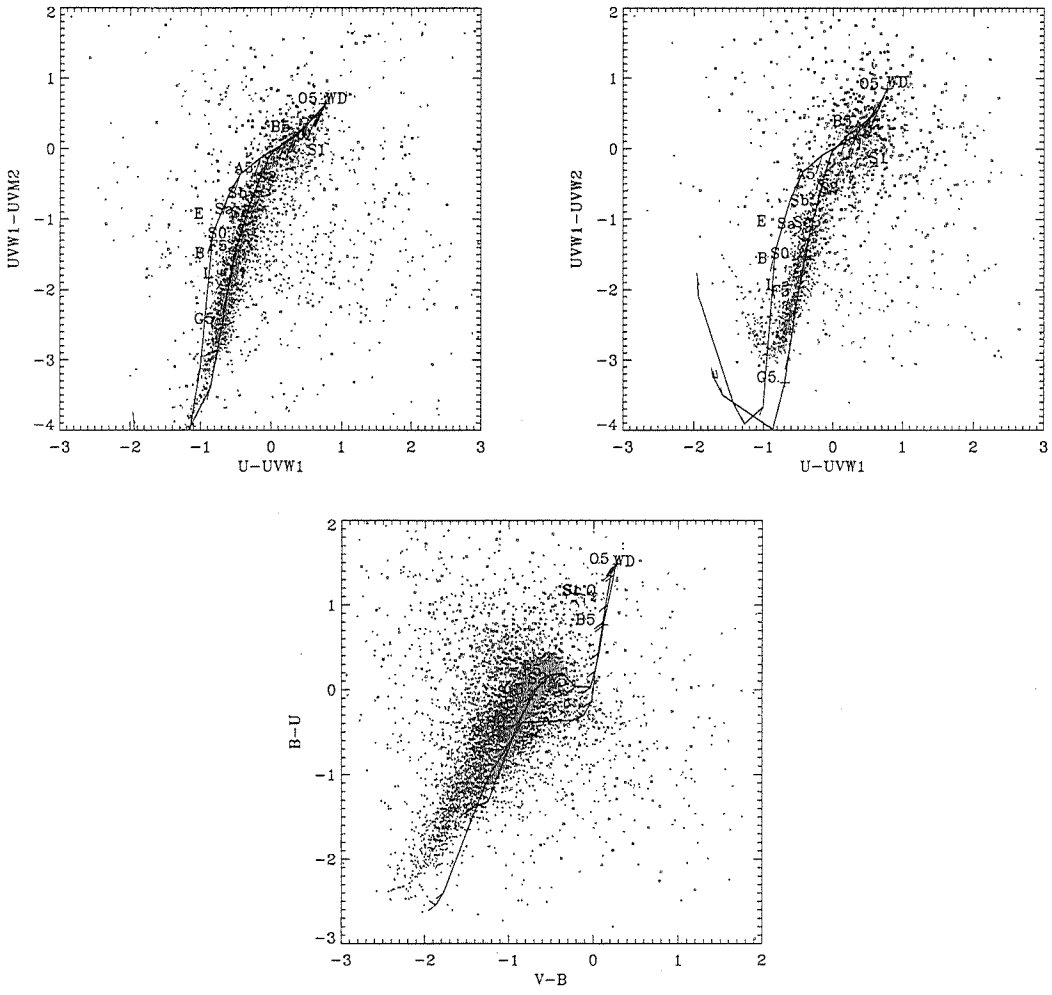

Fig. 10.— Color-color diagrams for the OM filters. Only sources with significances greater than 3 in each filter have been plotted. The thick solid line upon which the spectral types are indicated is the track of solar-metallicity dwarfs plotted with representative spectral types. The thin lines are reddening vectors for each spectral type assuming E(B-V)=0.1 and the Fitzpatrick (1999) reddening curve. No reddening corrections have been applied to the data. The other track (without spectral type indicators) is for solar-metallicity giants. Also marked is the location of white dwarfs (WD), QSOs (Q), Seyfert 1 and 2 (S1 and S2), typical galaxies (S0, Sa, Sb, Sc, and E) as well as spiral bulges. The dashed track is the path of QSOs from z=0 to z=1. Blue points are from fields with $|b| < 30°$, green points from fields with $30° < |b| < 60°$, and red points from fields with $60° < |b|$.

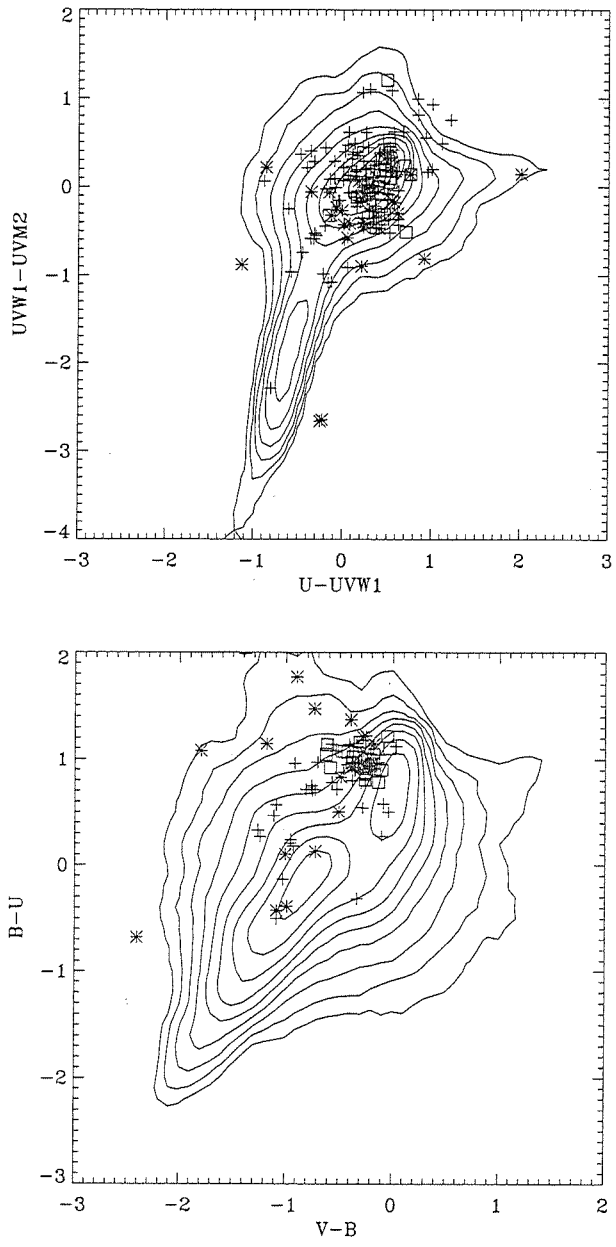

Fig. 11.— The contours of the source density of OMCat sources for $|b| > 30°$ are logarithmic. The location of QSO from the Veron catalogue (*red crosses*) the QSO from the SDSS catalogue (*green squares*) and the a mixed sample of QSO and galaxies that is the CfA redshift survey (*blue* $\times$).

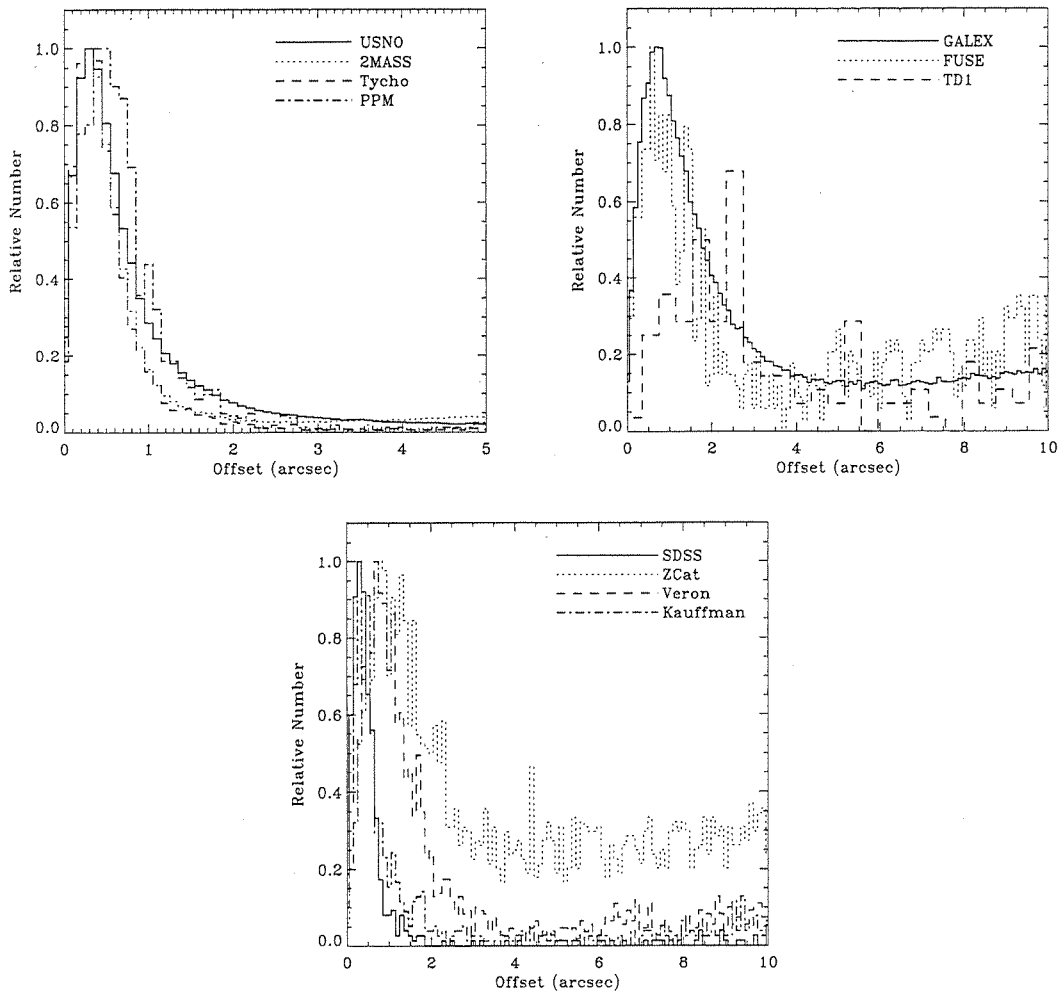

Fig. 12.— Each diagram is the distribution of the distance between sources in the OMCat and the nearest source in some other catalogue. **Left:** Catalogues dominated by stars and galaxies. **Middle:** Catalogues dominated by QSO and AGN. **Right:** Catalogues of UV sources. Note that since *FUSE* does not measure source positions (the positions were supplied by the user, typically from catalogues such as the Guide Star Catalogue) the width of the distribution for *FUSE* does not reflect the intrinsic accuracy of the *FUSE* pointing. The width of the distribution does still indicate the radius at which spurious matches become important.

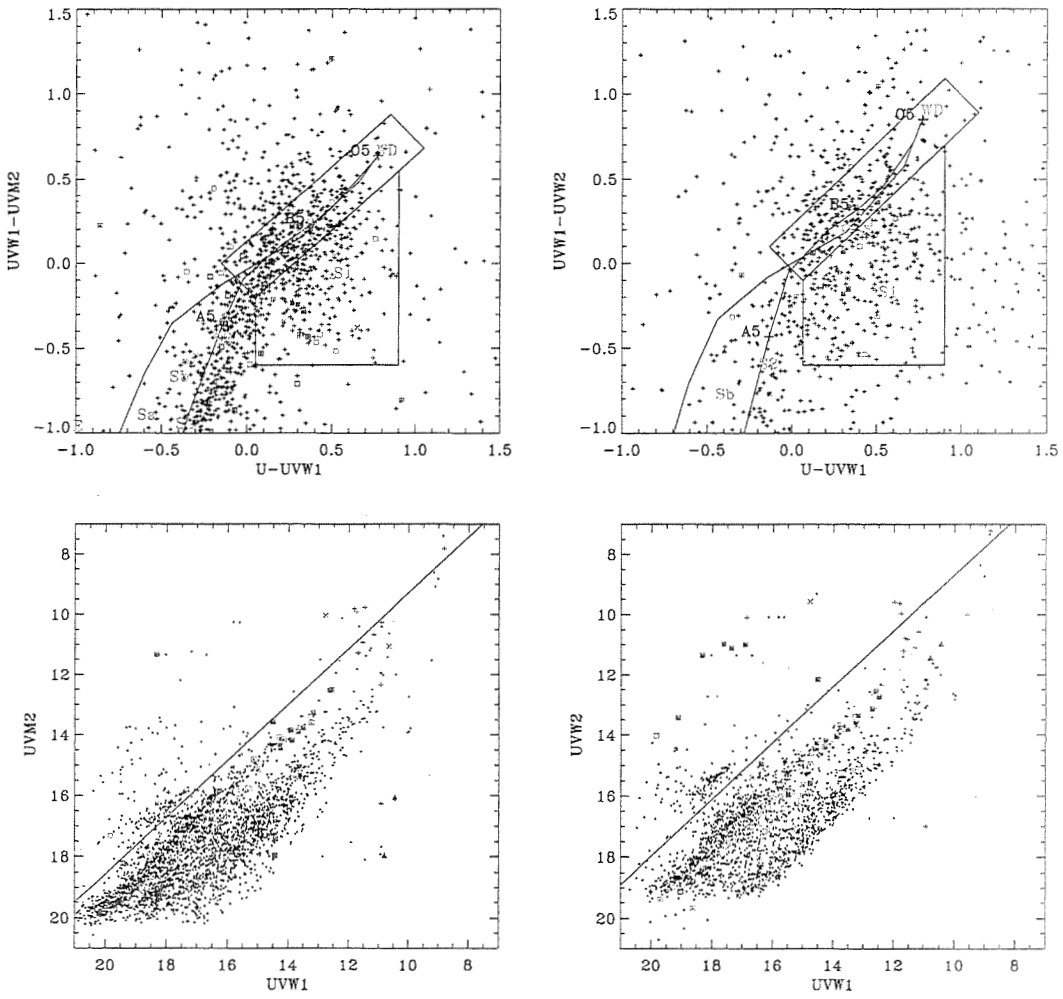

Fig. 13.— **Top Left:** The U-UVW1 *versus* UVW1-UVM2 color-color diagram, for all sources with $|b| > 46°$ and with detection significances greater than three and uncertainties < 0.1 mag in each band. *Red* symbols are sources observed by *FUSE*. Boxes are AGN, + are main sequence and giant stars, × are PN stars, Diamonds are white dwarfs, and Triangles are symbiotic stars. The source types are taken from the *FUSE* master catalogue. *Green* symbols are AGN from the Veron catalogue. *Blue* symbols are from the Sloan survey. *Purple* symbols are from the Kauffman/Sloan catalogue of AGN. The large boxes are the regions of interest for AGN (trapezoidal) and upper main sequence stars (rectangular). **Top Right:** The same plot for the U-UVW1 *versus* UVW1-UVW2 color-color diagram. **Bottom Left:** The UVW1 *versus* UVM2 diagram for the same sources. Note that there are three "sequences" of sources, the main one which runs almost along the diagonal which is composed of early type stars and AGN, a more diffuse band offset to the right which is composed of late type stars with UVW1-UVM2< -1.5, and a very short one to the left which is composed sources with UVW1-UVM2> 2.0; these are almost entirely spurious sources at the edge of the photocathode FOV. **Bottom Right:** The UVW1 *versus* UVW2 diagram for the sources in the U-UVW1 *versus* UVW1-UVW2 color-color diagram. The same three sequences are distinguishable.

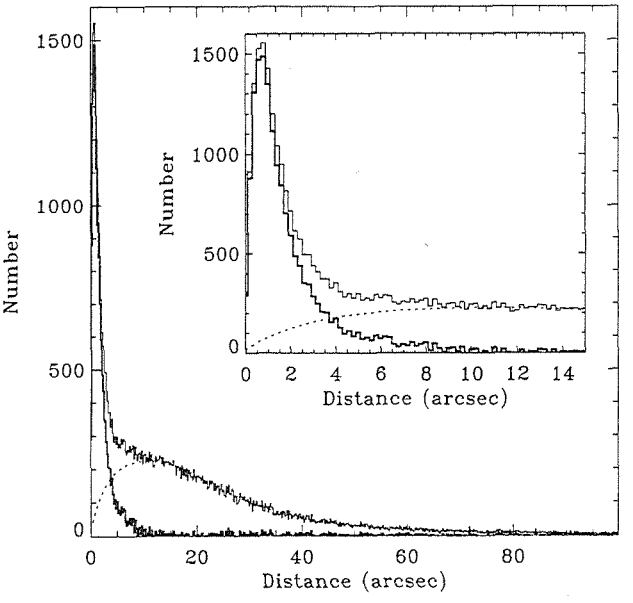

Fig. 14.— *Solid Histogram (black):* The distribution of the distance between an X-ray source and the closest OM source. *Smooth Curve (red):* The fitted probability distribution for the distance between the X-ray sources and the closest OM source for X-ray sources not correlated with OM sources (see text). *Dashed Histogram (blue):* The difference between those two distributions.

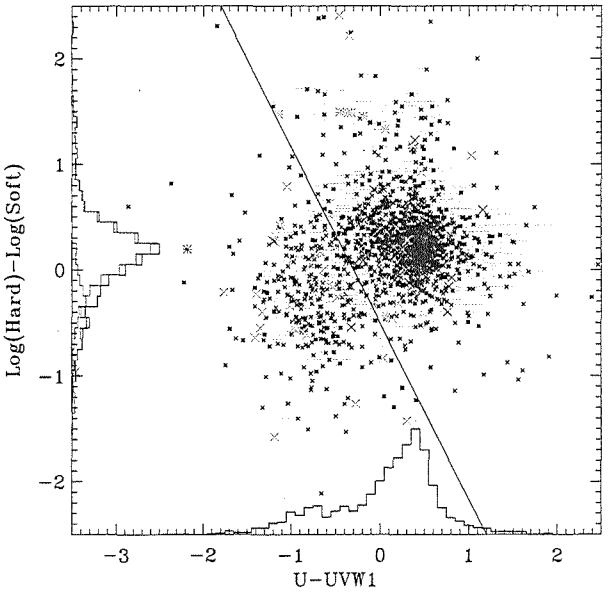

Fig. 15.— The UV color plotted against the $\log_{10}$ of the 2-12/0.5-2 keV X-ray hardness ratio for all sources with good UV or X-ray colors and $|b| > 30°$. For clarity, error bars are shown only when the Hard/Soft hardness ratio has a signal-to-noise ratio greater than 3 or the U-UVW1 uncertainty is < 0.477 magnitudes. The diagonal line separates the sources clustered around the "AGN" colors from those clustered around the "stellar" colors. Histograms of the projected distributions are shown along each axis. The distribution of the X-ray hardness ratio is plotted for all of the sources (black), the sources to the upper right of the line (blue), and to the lower left of the line (red). The **blue** symbols are SDSS sources classified as QSO, the **green** symbols are SDSS sources classified as galaxies, and the **red** symbols are SDSS sources classified as stars. Since the SDSS sources chosen for spectroscopy were selected to have a low probability of being stars, based on their colors and being unresolved, the low number of stars, and that fact that they have AGN-like colors, should not be surprising. The $\times$ indicate sources with good UV colors, the $+$ indicate sources with good X-ray colors, and source with both good UV and X-ray colors are marked with both symbols. For clarity, error bars equivalent to S/N< 3 are not shown.

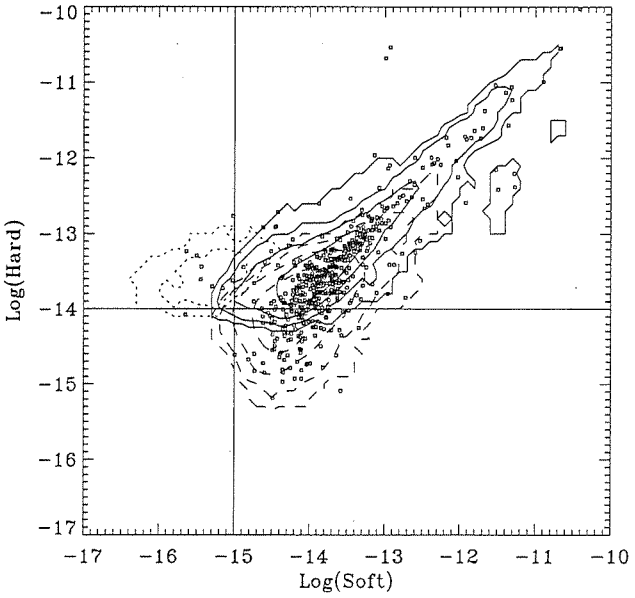

Fig. 16.— The contours show the density of sources from the entire SSC in the soft *versus* hard band parameter space. The fluxes are in erg cm^{-2} s^{-1}. **Green:** sources with 3σ detections in both bands, **Blue:** sources with 3σ detections in only the hard band, and **Red:** sources with 3σ detections in only the soft band. The points are sources with U-UVW1 colors.

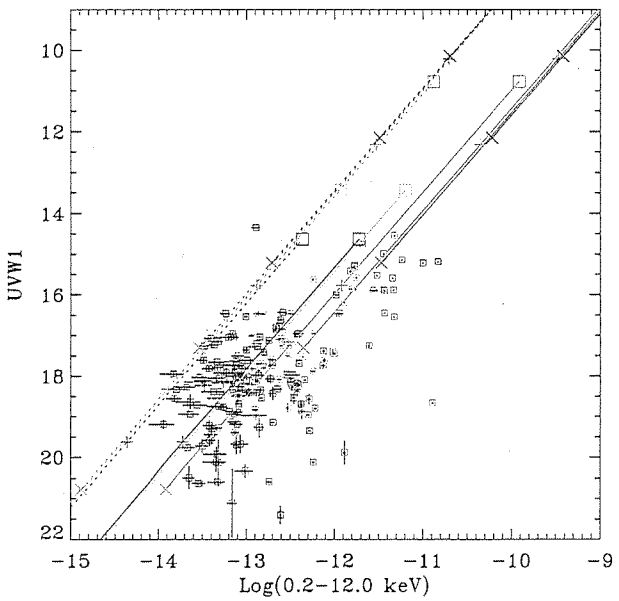

Fig. 17.— SSC sources with OM counterparts in the UVW1 band and AGN counterparts in the SDSS spectroscopic survey. **Small boxes:** sources are color-coded by redshift: $0 < z < 0.01$: purple, $0.1 < z < 0.04$: dark blue, $0.04 < z < 0.1$: light blue, $0.1 < z < 0.4$: green, $0.4 < z < 1.0$: orange, $1.0 < z$: red. **Solid lines:** the expected tracks for QSOs, color coded in the same manner as the sources; the large box denotes $L_{0.2-12.0keV} = 10^{47}$ ergs/cm^2/s, the large + denotes $L_{0.2-12.0keV} = 10^{45}$ ergs/cm^2/s and the large $\times$ denotes $L_{0.2-12.0keV} = 10^{43}$ ergs/cm^2/s. **Dotted lines:** the expected tracks for QSOs where the X-ray flux is absorbed by a column density of 10^{24} cm^{-2}.

Table 1. Catalogue Overview

Date	1 September 2006
Number of unique fields	2950
Number of sources with $\sigma > 3$	947638
Number of UV sources with $\sigma > 3$	508415
Number of sources in OM unique filters[a] with $\sigma > 3$	364741
Typical positional uncertainty	$< 0\farcs45$[b]

[a]The OM unique filters are UVW1, UVM2, and UVW2.

[b]As measured by the residual in position between matched OM and USNO sources. 50% of fields have uncertainties smaller than this value. The distribution of uncertainties peaks at $\sim 0\farcs3$.

Table 2. OM Filters

Name	λ_0[a] (Å)	λ_{max}[b] (Å)	FWHM (Å)	PSF FWHM (arcsec)	Peak Mag.
V	5407	5230	684	1.35	19.0
B	4334	3980	976	1.39	19.7
U	3472	3270	810	1.55	19.5
UVW1	2905	2680	620	2.0	19.3
UVM2	2298	2210	439	1.8	18.3
UVW2	2070	2000	500	1.98	17.6
WHITE[c]					22.2

[a]Effective wavelength

[b]Wavelength of maximum transmission

[c]An "open" filter

Table 3. OM Color Statistics Number of 3σ Detections[a]

Filter	V	B	U	UVW1	UVM2	UVW2	WHITE
V	1028785	233685	207608	165249	79448	56517	1867
B	233685	548128	225180	133163	60190	66840	4600
U	207608	225180	651438	247353	84993	62469	3546
UVW1	165249	133163	247353	768349	144107	76204	2807
UVM2	79448	60190	84993	144107	256142	79766	950
UVW2	56517	66840	62469	76204	79766	191067	359
WHITE	1867	4600	3546	2807	950	359	11095
X-ray Selected Sources							
V	8536	2585	2732	2720	644	491	56
B	2585	9694	4978	3964	803	685	403
U	2732	4978	15278	7016	1451	864	375
UVW1	2720	3964	7016	25477	2829	1852	334
UVM2	644	803	1451	2829	6459	1467	143
UVW2	491	685	864	1852	1467	7521	70
WHITE	56	403	375	334	70	143	812

[a]For colors, the requirement was that both detections be greater than 3σ, not that the color be measured to a signal-to-noise of 3.

Table 4. Cross-Correlations

Catalogue Name	Entries	Matches	Coordinate Uncertainty[a]	Match Peak	Match Width	Match Radius
USNO B-1	1045913669	455481	0.″2	0.303	0.199	0.702
2Mass	470992970	265991	0.″06	0.255	0.162	0.580
Palomar-Green	1878	...	8″	...	...	...
Tycho-2	2539913	5322	0.06	0.271	0.189	0.650
PPM	468861	1177	0.″3	0.469	0.309	1.087
SAO	258944	578	$\sim 2''$	0.920	0.478	1.876
CfA Z Cat	58738	1366	1″[b]	1.470	0.574	2.619
Veron	108080	1099	1″[b]	0.706	0.341	1.388
SDSS NBC QSO	100563	395	0.36mas[b]	0.323	0.210	0.742
GALEX	110236958	42528	1″	0.647	0.349	1.346
FUSE	4037	376	1.″5[c]	1.225	0.442	2.109[c]
TD1	31215	82	0.″2[b]	2.036	1.089	4.215

[b]From catalogue documentation accessed through the HEASARC.

[b]Precision of coordinate as the uncertainty was not quoted.

[c]Since the FUSE catalogue is of observed targets, the coordinates are presumably those provided by the observers. The smallest aperture in use has a width of 1.″5 while the medium aperture has a width of 4.″0, suggesting that the coordinates are at least this good in order to make a successful observation.